Jurnal Kejuruteraan 38(4) 2026: 2025-2042
https://doi.org/10.17576/jkukm-2026-38(4)-37

Design Optimization of Tri-Spiral Windings Based on Electromagnet Designs for Stator Coreless Axial Flux Generator

Isiaka Shuaibu[a,b*], Eric Ho Tatt Wei[a,b] & Ramani Kannan[a]

[a]*Departement of Electrical and Electronics Engineering, Universiti Teknologi PETRONAS, 32610 Seri Iskandar Perak, Malaysia.*

[b]*Centre for Intelligent Signal & Imaging Research, Universiti Teknologi PETRONAS, Malaysia*

[*]*Corresponding author: isiaka_22000514@utp.edu.my*

Received 17 May 2025, Received in revised form 4 March 2026
Accepted 4 April 2026, Available online 30 July 2026

ABSTRACT

Coreless windings are highly promising for both low and high-speed axial flux permanent magnet machines, offering distinct advantages over traditional cored windings. Their ability to be freely arranged within the airgap provides extensive opportunities for optimizing lightweight generator designs. Despite this potential, research on coreless windings remains limited. This study deviates from conventional winding and permanent magnet designs, demonstrating that generator performance can be significantly enhanced by refining winding geometry and electromagnet configuration. A tri-spiral coil (TR-SPC) with uniform turns was designed alongside two electromagnet configurations: a trapezoidal-shaped electromagnet (TR-ELMAG) and a dual spiral electromagnet (DR-ELMAG) to investigate these improvements. The analytical design methodology is first presented and subsequently verified through finite element analysis (FEA) using ALTAIR Flux® v2022.3. The electromagnetic performance was evaluated on a single-stator, double-rotor coreless axial flux electromagnet generator (SSDR CAFEMG) using both ferromagnetic and non-ferromagnetic materials at 500 rpm and 50 Hz. Notably, the results indicated that the DR-ELMAG configuration outperforms TR-ELMAG across most metrics, achieving an airgap flux density of 495.25 mT and a coil flux density of 478.65 mT, compared to 194.42 mT and 224.72 mT for TR-ELMAG. Further evaluation shows that DR-ELMAG delivers a higher average torque of 1.15 Nm, zero cogging torque, output power of 166 W, and efficiency of 92.2%, in contrast to TR-ELMAG, which produces 0.18 Nm of torque, 34 mNm of cogging torque, 164 W of output power, and 91.1% efficiency. Future work will focus on prototype fabrication, load-based experimental validation, and comprehensive thermal modeling to improve scalability.

Keywords: Coreless Axial flux PM generators; electromagnet; finite element analysis; spiral coil design; power quality

INTRODUCTION

Among permanent magnet generators, the axial flux permanent magnet generator (AFPMG) is distinguished by its significantly shorter axial length compared with the radial flux permanent magnet generator (RFPMG) (Habib et al., 2020). Owing to their inherent structural and electromagnetic advantages, AFPMG are increasingly replacing RFPMG counterparts in a wide range of applications. These advantages include high efficiency, high power density, compactness, and reduced manufacturing cost (Shuaibu et al. 2024b; El-Hasan, 2023). Consequently, axial flux technology has attracted considerable research interest for applications requiring lightweight and high-performance electrical or mechanical energy conversion (Zaihidee et al. 2022; Mohd Nasir et al. 2025).

AFPMG can be realized in several configurations, including single-sided, double-sided, and multi-disk topologies (Shuaibu et al. 2024b). Among these, the double-sided configuration where the stator winding is sandwiched between two permanent magnet rotors is particularly attractive due to its superior power density and balanced electromagnetic performance, making it suitable for high-performance applications.

Coreless AFPMGs are increasingly explored for renewable energy systems and other advanced applications due to their distinctive electromagnetic characteristics (Shuaibu et al. 2024a; Wang et al. 2022; Shuaibu and Wei Ho 2023). By eliminating iron in both the stator and rotor, coreless designs remove iron losses and significantly reduce eddy current losses. In addition, the absence of iron mitigates magnetic pull forces between the stator and rotor, contributing to improved mechanical stability (Zhu et al. 2023). Despite these benefits, coreless AFPMGs face notable challenges. These include complex mechanical structures, higher material costs, unstable axial forces in poorly balanced designs, and increased reliance on high-energy permanent magnets (Shuaibu and Wei Ho, 2023). These factors can partially offset the electromagnetic advantages of coreless configurations if not carefully addressed.

One of the most compelling features of AFPMG is its geometric flexibility. The machine support a wide range of rotor pole and armature coil shapes, including trapezoidal, cylindrical, and semi-cylindrical magnet topologies, each of which strongly influences magnetic flux distribution, structural integrity, and manufacturing cost (Wang et al. 2022; Frank and Laksar 2021; Alsuwian et al. 2024; Pranjic and Virtic 2020; Alsuwian et al. 2025). Similarly, stator windings may adopt trapezoidal, circular, or rhomboidal coil geometries, offering extensive freedom for electromagnetic optimization (Shuaibu et al. 2025). AFPM machines also accommodate both non-overlapping concentrated windings and overlapping non-concentrated windings.

However, despite the breadth of available configurations, existing literature often treats winding topology as a secondary design variable, with limited systematic investigation into its impact on flux waveform quality, harmonic content, induced EMF characteristics, and overall generator performance particularly in coreless double-sided AFPMG architectures. This represents a significant research gap in the current state of AFPMG development.

While most studies focus on permanent magnet excitation, emerging research has begun exploring electromagnet-based designs as alternatives for reducing dependence on rare-earth materials and improving controllability, most especially with proof of concept (Devred et al., 2024; Lijesh & Hirani, 2015). These designs introduce additional degrees of freedom in flux regulation but also increase system complexity, excitation losses, and control requirements. Accurate electromagnetic modelling, especially capturing three-dimensional field effects, remains a critical challenge and open area of research for both permanent magnet and electromagnet-based AFPMG.

In response to the identified challenges and gaps, this work focuses on advancing coreless axial flux electromagnet generator (CAFEMG) design through a systematic investigation of winding topology and electromagnet-based configuration. The contributions to this paper are summarized as follows:

1. A single-layer planar coil is proposed to enhance the electromagnetic performance of single stator double rotors CAFEMG, providing improved magnetic flux density.
2. A dual-electromagnet structure based on trapezoidal and spiral geometries (TR-ELMAG, DR-ELMAG) is designed to achieve enhanced magnetic field uniformity while minimizing harmonic distortion in the back electromotive force (BEMF).
3. A hybrid electromagnet-planar winding configuration based is developed to mitigate torque imbalance and significantly improve power quality, thereby enhancing stability.
4. Implementation of FEA-based simulation via Altair Flux 2022.3

The organization of the paper is as follows: the literature review is presented first, followed by the adopted methodology detailing the design and analysis of the electromagnet-based generator (CAFEMG). Thereafter, the results and discussion are presented, and the paper concludes with conclusions and recommendations for future work.

LITERATURE REVIEW

Recent research has introduced several innovative designs and optimization techniques to address these challenges. One of such approach involves spiral coil designs and concentric winding configurations, which improve performance by achieving optimal performances with shortcomings. Research conducted by Shuaibu and Wei Ho (2023), a novel dual spiral coil design was presented with overlapping coil design achieving the highest output of 92W at 500rpm. Both designs produced steady-state sinusoidal voltage and current with little transient distortion at the initial stage. A study by Huang et al. (2023) introduces a novel concentric winding axial-flux permanent magnet machine with a high winding factor of 1 and short winding ends. The stator is divided into three concentric circles, with phase differences achieved through mechanical offsets. Balanced back EMFs and strong overload capability were achieved using three-dimensional finite element analysis (3D FEA), with theoretical analysis modeling fan-shaped slots and neglecting radial flux leakage.

In research conducted by Gao et al. (2024a) presents an analytical model and optimization for a coreless axial flux permanent magnet motor with a PCB stator, achieving 3% higher efficiency with an arc-shaped distributed winding compared to a concentrated winding. The optimized motor, validated through prototype testing, achieved over 90% efficiency at 1500 rpm and 0.85 Nm, requiring further improvement. Chulaee and Ionel (2024) propose a computationally efficient 3D FEA model with planar PCB stators for the same machine topology, reducing computational burden while maintaining accuracy. The model leverages geometric symmetry and proposes a systematic approach to minimize FEA solutions, validated by experimental back-EMF and output torque results. It's suitable for machines with low saturation and cogging torque effects.

Similarly, Marcolini et al. (2023) presented a multiphysics design approach for coreless axial flux permanent magnet machines with concentrated windings, emphasizing optimization of the rotor pole–stator coil ratio. Fast 2D analytical models were used for rapid design evaluation, followed by 3D FEA for final optimization. Experimental validation achieved a torque density of 2.12 Nm/kg and a peak efficiency of 87%. However, the study focused solely on permanent magnet excitation and did not extensively address cost or scalability.

This study Shang et al.(2024) employs a skewed wave winding design that optimizes the inner diameter and reduces the radial length, improving propeller size and efficiency of motor. The results showed that increasing the pole count improved efficiency by reducing copper losses and optimizing winding lengths. Ultimately, the 16- pole motor met design requirements and performed effectively, offering a promising solution for shaftless rim thrusters in underwater robotics. Future research aims to enhance motor efficiency and performance further.

The work of Gao et al. (2024b) introduces an optimization approach for dual rotor coreless stator permanent magnet machines with non-overlapping concentrated windings. Optimizing the pole number to exceed the slot number increases torque output by 34.8%, with further improvements from optimizing the Halbach PM array. The study notes that 2D FEA models may not fully capture 3D effects, necessitating 3D FEA for accurate optimization. Authors Aghapour et al. (2023) investigated the performance of a CAFPMG with different rotor positions. Position 3 yields the best performance with the lowest harmonic, while Position 1 achieves the highest back-EMF and torque. The study highlights the trade-offs between these characteristics and notes the need for more accurate EMF and harmonic distortion studies.

Author Ouldhamrane et al. (2022) presents a fast and accurate 3D modelling method for evaluating the electromagnetic performance of axial flux permanent magnet machines under no-load conditions. This method combines magnetic charges, image theory, and relative permeance functions, which were validated with a prototype and agreed well with experimental results. Still, improvements are required for nonlinear magnetic material saturation and better capture of magnetic field concentration effects. Table 1 gives an overview of coreless design based on the methodological approaches, winding topology, magnet array, coreless design, AFPM topology and materials.

From the reviewed literature, optimization efforts have largely focused on permanent magnet excitation with various winding topologies, while hybrid electromagnet excitation combined with a tri-spiral winding topology in coreless axial flux permanent magnet generators (CAFPMG) remains unexplored. Existing designs also exhibit limitations in flux concentration efficiency and coil surface utilization, which affect torque, power output, and EMF waveform quality. This study addresses these gaps by proposing and analyzing a hybrid electromagnet-based CAFEMG incorporating a tri-spiral coil topology. The proposed approach improves air-gap flux distribution, enhances coil utilization, and reduces harmonic distortion through accurate electromagnetic modeling and comparative analysis.

TABLE 1. Summary of Configuration Methods and Materials

Ref.	Methods	Winding & PM Array	Coreless Design / Topology	Materials	Limitations
Habib et al. (2020)	Analytical & FEM	CTW and Trapezoidal PM with Con and Halbach	Fully coreless / MSMR	Epoxy resin	Both current and voltage waveforms exhibited transient distortions needing further improvement.
Frank and Laksar (2021)	Analytical, FEM & Prototype	Planar CTW and Trapezoidal PM with Conventional	Stator coreless / SSDR	Iron, Copper	Although the pico generator is accompanied by non-perfect sinusoidal flux density and high cost due to materials usage.

continue...

...cont.

Alsuwian et al. (2024)	Analytical, FEM & Prototype	CTW and Trapezoidal PM with Conventional and Halbach	Fully coreless / DSSR, SSDR and MSMR	Polycarbonate 3D filament, Acrylonitrile butadiene styrene (ABS) 3D filament	High consumption of neodymium iron boron (NdFeB) permanent magnet limits the utilization for rural electrification with high cost implications.
Marcolini et al. (2023)	Analytical, FEM & Prototype	CTW and Sector-like PM with Conventional	Stator coreless / SSDR	FR4-core, Fibreglass	PM shaping and retainment demonstrated optimal performance but can be susceptible to stator eddy current or heat loss.
Wang et al. (2022)	Analytical & FEM	CTW and Trapezoidal PM with Conventional	Stator coreless / SSDR	Not Available	The wedge-shaped coil achieved by rolling technology performs exceptionally and can be refined with a 3D planar coil to improve the electromagnetic performance.
Pranjic and Virtic (2020)	Analytical, FEM & Prototype	CTW and Sector-like PM with Conventional	Stator coreless / SSDR	Printed SMC	Study majorly focused on rotor deflection.
Tsunata et al. (2022)	Analytical & FEM	CTW and Trapezoidal PM with Conventional and Halbach	Rotor coreless / DSSR	Non-magnetic material HBX	Design experienced low permeability due to SMC materials usage with a wide air gap
Proposed	Analytical & FEM	Tri-spiral CTW, Trapezoidal, and dual reversal electromagnets	Stator coreless / SSDR	Epoxy resin, Polyamide, Bakelite, and iron	-

METHODOLOGY

GENERATOR STRUCTURE AND MODELING

The proposed generator adopts a coreless single-stator double-rotor (SSDR) axial flux configuration with a dual symmetrical disc architecture, and its key parameters are summarized in Table 2. Two rotor discs, each carrying circumferentially arranged electromagnets, with a central coreless stator to form a 12-electromagnet pole machine. This arrangement enables axial flux to traverse the air gap and effectively link with the stator windings. For analytical modelling and dimensional estimation, established AFPM design approaches are adopted. In particular, the diameter of the AFPMG is computed using an improved formulation presented by Shuaibu and Wei Ho (2023); Minaz and Çelebi (2017), as expressed in (1), providing a validated baseline for the outer diameter geometry of 220mm and electromagnetic analysis.

$$D_{ot} = \sqrt[3]{\frac{\epsilon P_g}{\pi^2 K_D \rho N_s B_g E_l \eta \cos\emptyset}} \qquad (1)$$

Where ∈ stands for the generator value, which is greater than 1, assumed as 2, P_g is the input power, K_D is the distribution factor, ρ is the winding factor of 0.95, N_s is the rated speed of 500 rpm, B_g is the assumed airgap magnetic flux density for the electromagnet of 0.5T, E_l is the electrical loading, η is the efficiency of 90% and cosØ is the power factor of 1, respectively.

The electrical loading (E_l) in A/m is further expressed following Habib et al. (2020), as given in (2).

$$E_l = \frac{4mN_{cm}I_{cm}}{\pi D_{ot}(1+\lambda)} \qquad (2)$$

Where m is the number of phases, N_{cm} and I_{cm} are the number of turns and current per phase. To further improve AFPMG, machine sizing equations known as distribution factor was employed by (Khan et al. 2019), which is given by equation (3):

$$K_D = \frac{1}{8}(1-\lambda)(1+\lambda^2) \qquad (3)$$

To obtain the rotor and stator inner geometrical diameter dimensions, we employed equation (4) as follows:

$$D_{it} = \lambda\, D_{ot} \qquad (4)$$

While λ is the ratio of inner to outer diameter with an optimal value of 0.58 utilized mostly in the literatures by Habib et al. (2020) and Shuaibu and Wei Ho (2023). However, to accommodate the tri-spiral coil for this design, a value of 0.41 was employed, resulting in an inner rotor diameter of approximately 90mm respectively.

TABLE 2. Tri-spiral Coil (TR-SPC) Generator Design Constraints

Parameter/unit	Symbol/Units	Specification
Number of phases	m (-)	3
Rated input power	P_g (W)	180
Rated speed	N_S (rpm)	500
Airgap (mm)	ag (mm)	0.5*2
Outer diameter (mm)	Dot (mm)	220
Inner diameter (mm)	D_{it} (mm)	90
Frequency	f (Hz)	50

Figures 1 and 2 depict the coreless configuration and overall design flowchart, respectively.

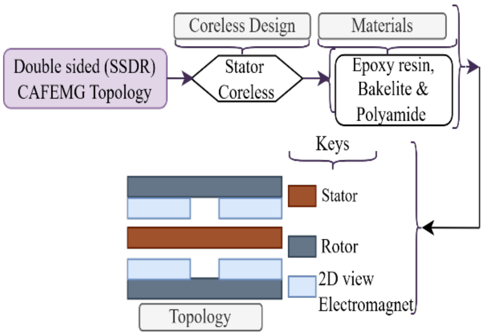

FIGURE 1. Schematic representation of Stator CAFEMG based on SSDR Configurations.

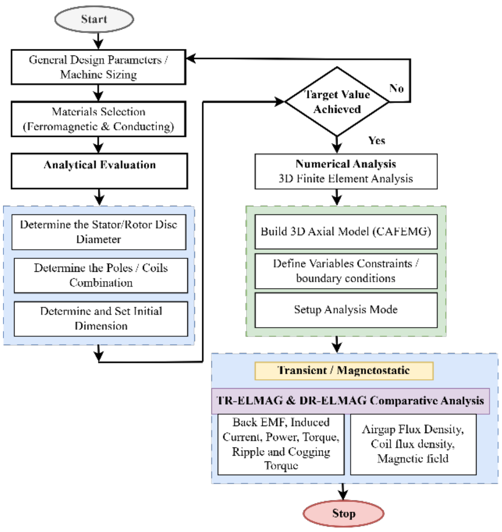

FIGURE 2. Flowchart of the Electromagnet-Based Methodology for CAFEMG

PLANAR COIL WINDING

Spiral planar concentrated windings are adopted due to their manufacturing simplicity and compatibility with CAFEMG, as they eliminate complex end-turn geometries and improve copper fill factor. A single-layer stator with an a–b–c phase arrangement is used, where three coils span four poles to enhance flux linkage and induced EMF characteristics. The planar tri-spiral topology ensures uniform current distribution and efficient utilization of the available air-gap area.

For CAFEMG, a single-layer modular winding configuration comprising nine coils and twelve pole pairs is selected. The corresponding phase connections and coil sequencing are provided in Table 3 and are used directly in the electromagnetic modelling and performance evaluation.

TABLE 3. 3-Phase Winding Connection.

Coil Number	1	2	3	4	5	6	7	8	9
Connection	A	-A	A	B	-B	B	C	-C	C

TRI-SPIRAL COIL (TR-SPC) DESIGN FLOWCHART

Figure 3 illustrates the three-phase methodology used for the design, configuration, and validation of the TR-SPC coil, with each phase structured to ensure compliance with functional and modelling accuracy requirements.

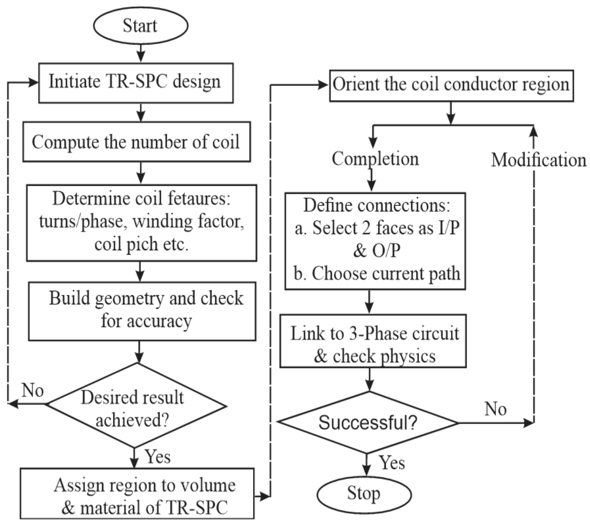

FIGURE 3. Research flowchart for tri-spiral (TR-SPC) coil design, configuration, and validation

The TR-SPC design follows a three-phase methodology. First, the coil geometry is defined by determining the number of coils, turns per phase, and winding parameters, followed by geometric validation against modelling constraints. Next, coil regions and volumes are assigned, and material properties such as conductivity, permeability, and resistivity are specified, with conductor orientation aligned to the intended current path. Finally, the coil is integrated into a 3-phase circuit, where terminal connections and current paths are defined, and phase A, B, and C parameters are computed, such as resistance (R) and inductance (L), respectively taking coil conductor (C) into consideration.

$$R = R_A = R_B = R_C \tag{5}$$

$$L = L_A = L_B = L_C \tag{6}$$

$$C = C_A = C_B = C_C \tag{7}$$

Model consistency and physics checks are then performed to verify electromagnetic behaviour, yielding a validated coil configuration for generator analysis, as illustrated in Figure 4.

TABLE 4. 3 Phase Circuit parameters

Parameters	Units	Values
Resistance (R)	mΩ	0.1
Inductance (L)	mH	0.159

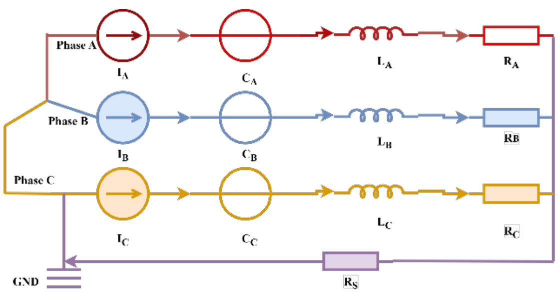

FIGURE 4. 3-phase equivalent circuit design for tri-spiral (TR-SPC) winding.

The computation for the designated parameters follows these equations (8) – (10).

$$R = \frac{2\pi r_{av} N\rho}{A_c} \tag{8}$$

$$r_{av} = \frac{1}{2} \cdot \frac{D_{ot}+D_{it}}{2} \tag{9}$$

The surface area of the coil (A_c) is given as in equation (10). The active length per turn reduces linearly and is governed by the conductor width and inter-track clearance. The coil area for a uniform copper-trace spacing is evaluated using (10), where the first term denotes the effective coil area and the second term represents the cumulative clearance between successive turns.

$$A_c = \pi\left[\frac{(D_{oc}+D_{ic})^2}{4} + (S_c \times W_c)\right] \tag{10}$$

Where the D_{oc} and D_{ic} duly represent the outer and inner diameters of TR-SPC coil, respectively. The coil spacing is defined by (S_c), coil thickness represents (W_c) and N is the number of turns.

Similarly, the coil inductance is computed using the expression given in (Hussain and Woo, 2022), as presented in (11), with minor modifications to accommodate the present design. In particular, the average coil diameter d_{av} is incorporated, as defined in (12), to ensure accurate inductance estimation.

$$L = \mu_o N^2 d_{av}\left[\ln\left(\frac{2.46}{\rho}\right) + 0.2\rho^2\right] \tag{11}$$

Where the permeability of free space ($4\pi \times 10^{-7} H/m$).

$$d_{av} = \frac{D_{oc}+D_{ic}}{2} \tag{12}$$

DEVELOPMENT PROCESSES OF TRP-SC GEOMETRY

The TR-SPC follows a structured and iterative modelling procedure comprising geometry definition, material assignment, and circuit integration. At each stage, validation checks are performed to identify and correct geometric or electromagnetic inconsistencies before proceeding, thereby improving modelling accuracy and reducing cumulative errors. The TR-SPC is configured as three planar spiral arms arranged in an interlocking circular pattern, as shown in Figure 5. This geometry is selected to improve air-gap surface utilization and promote uniform circumferential flux linkage. The winding incorporates a dual-conjoined via and a single mono via to ensure electrical continuity while maintaining geometric symmetry. All spiral arms follow an anticlockwise orientation to preserve a consistent current direction and phase balance.

Each coil consists of eighteen turns uniformly distributed among the three spiral arms, resulting in six turns per arm converging at a common junction. This distribution is chosen to balance flux linkage and phase symmetry while limiting conductor overlaps. The corresponding winding separation angle is analytically defined in (13) and is used directly in the electromagnetic model.

$$\theta = {}^{360}/_{N_c} = 40 \tag{13}$$

But $N_c N_c$ and C is the total number of coils and cores, further expressed as in equation (14)-(15).

$$N_c = {}^{3}/_{4} \times C \tag{14}$$

But

$$C = 60\frac{f}{N_s} \tag{15}$$

Where *C* denotes the number of pair cores for a single rotor, *f* is the operating frequency, and N_s is the rated speed. The number of turns is computed using (16), with I_p representing the peak current (3.5A), D_{ot} the outer stator diameter, a_w the number of parallel current paths (6) with two per each coil arm, *m* the number of phases (3), and N_{cm} the number of coils per phase (3).

$$N = \frac{\pi a_w D_{ot}(1+\lambda)E_l}{4N_{cm}I_p} \tag{16}$$

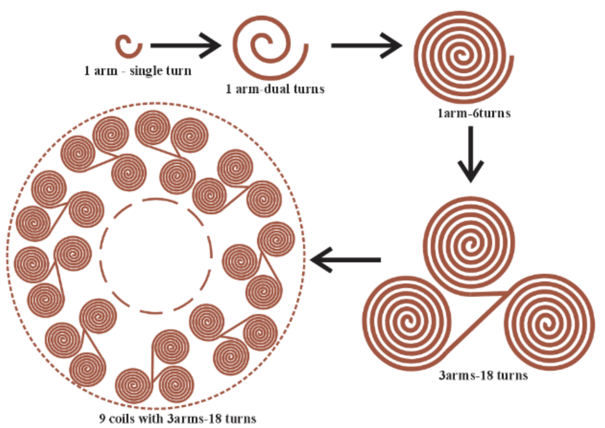

FIGURE 5. Implementation of a single-layer TR-SPC Coil geometry for stator coreless design

The Tri-spiral Coil (TR-SPC) for CAFEMG design constraints is presented in Table 4

TABLE 4. Tri-spiral Coil (TR-SPC) Generator Design Constraints.

Parameter/unit	Symbol/Units	Specification
Axial height (mm)	a_h (mm)	3
Connections	-	3
Coil outer diameter	D_{oc} (mm)	54
Coil inner diameter	D_{ic} (mm)	1.5
Number of coils	N_c (-)	9
Winding turns	N (-)	18
Winding layers	w_l (-)	1
Clearance	S_c(mm)	1.26
Width	w_c (mm)	0.75

FUNDAMENTAL STRUCTURE OF ELECTROMAGNETS

In this analysis, an electromagnetic equivalent circuit is developed for two electromagnet configurations comprising 12-coil and 6-coil units, based on trapezoidal and dual-reversal spiral geometries, respectively, as shown in Figures 6 and 7. Each electromagnet pair is integrated on a shared core and positioned symmetrically on the upper and lower rotor regions.

The electromagnetic assembly consists of a trapezoidal core, trapezoidal coil, dual-reversal spiral coils, and a rotor base. Both electromagnet designs operate with a coil current of 2.3 A supplied by five series-connected 12 V DC sources (60 V) as in Figure 6. The air gap between adjacent electromagnets is maintained at 3 mm. Key parameters of the trapezoidal electromagnet (TR-ELMAG) and dual-reversal electromagnet (DR-ELMAG) are summarized in Table 5.

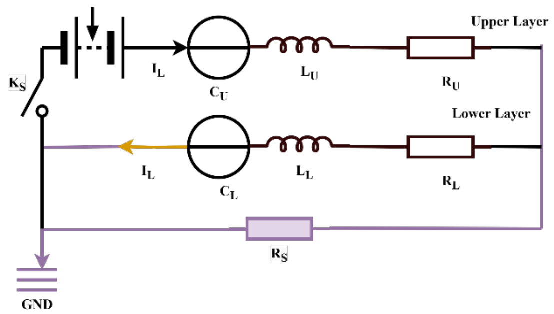

FIGURE 6. Adopted Electromagnet Excitation Circuit

The switch K_s controls the excitation of the electromagnets, allowing current flow when closed and rendering the electromagnet inactive when open. The upper and lower rotor phase parameters are assumed identical, with equal resistances ($R_u = R_L$), inductances ($L_U = L_L$), and ground resistance (R_s). However, the critical geometrical parameters influencing the performance of the electromagnet core and coil are summarized in Table 5 with reference to Figures 7(a)-(b), while Figures 7(c)-(d) illustrate the layout of the trapezoidal electromagnet (TR-ELMAG) and dual-reversal electromagnet (DR-ELMAG) on the rotor base.

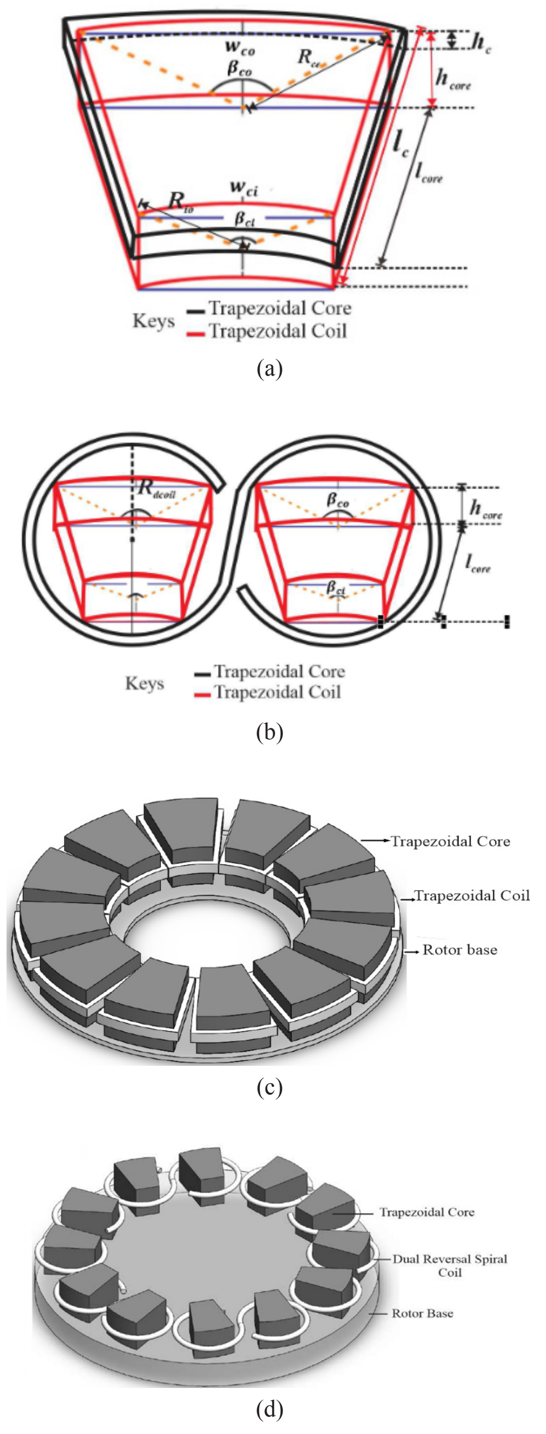

FIGURE 7. Electromagnet configurations design and structural layout (a) TR-ELMAG design (b) DR-ELMAG design (c) TR-ELMAG layout, (d) DR-ELMAG layout

The corresponding coil phase parameter values used for the electromagnets are identical to those of the TR-SPC coil.

TABLE 5. Specification of the Electromagnets

Parts	Parameters	TR-ELMAG	DR-ELMAG
Coil	Inner diameter of the coil (mm)	-	51
	Outer diameter of the coil (mm)	-	76
	Inner width (W_{ci}) of the coil (mm)	22	-
	Arc inner angle (β_{ci})	21	-
	Outer width (W_{co}) of the coil (mm)	51	-
	Arc outer angle (β_{co})	49	-
	Length of coil (mm)	18	-
	Height of coil (mm)	5	5
	Thickness (mm)	6	6
	Number of turns	18	18
Core	Inner core width (W_{ci}) (mm)	13	6.5
	Arc inner angle (β_{ci})	15	15
	Outer core width (W_{co}) (mm)	40	20
	Arc outer angle (β_{co})	42	42
	Height of core (mm)	7.5	7.5
	Length of core (mm)	52	-
	Number of cores	12	6
	Material of the core	Iron	Iron

ELECTROMAGNET DESIGN FLOWCHART

Figure 8 presents the structured design workflow for the trapezoidal electromagnet (TR-ELMAG) and dual-reversal electromagnet (DR-ELMAG). The process begins with the initialization of a 3D transient magnetic simulation. The core geometry is defined using specified dimensions, including top and bottom bases, height, and slanted edges, to preserve the trapezoidal profile. Material properties, such as magnetic permeability, are assigned to the core using soft iron based on their magnetic characteristics. For each configuration, magnetic path length, air-gap parameters, and coil geometry are computed. The TR-ELMAG and DR-ELMAG are then modeled by defining winding structures, extrusion parameters, and origin offsets, while the number of turns is calculated using analytical expressions to control resistance and conductor length.

The winding region is subsequently excited using a DC voltage source, and the resulting current is coupled to a two-phase equivalent circuit for validation, as shown in Figure 6. Magnetic field solutions within the core and air gap are obtained using 3D finite element analysis to evaluate flux density and field strength. Geometry, material assignment, and magnetic performance are iteratively validated to ensure modelling consistency. The resulting configurations are used to enhance magnetic flux distribution and electromagnetic performance of the SSDR CAFEMG through the combined application of TR-ELMAG, DR-ELMAG, and TR-SPC windings.

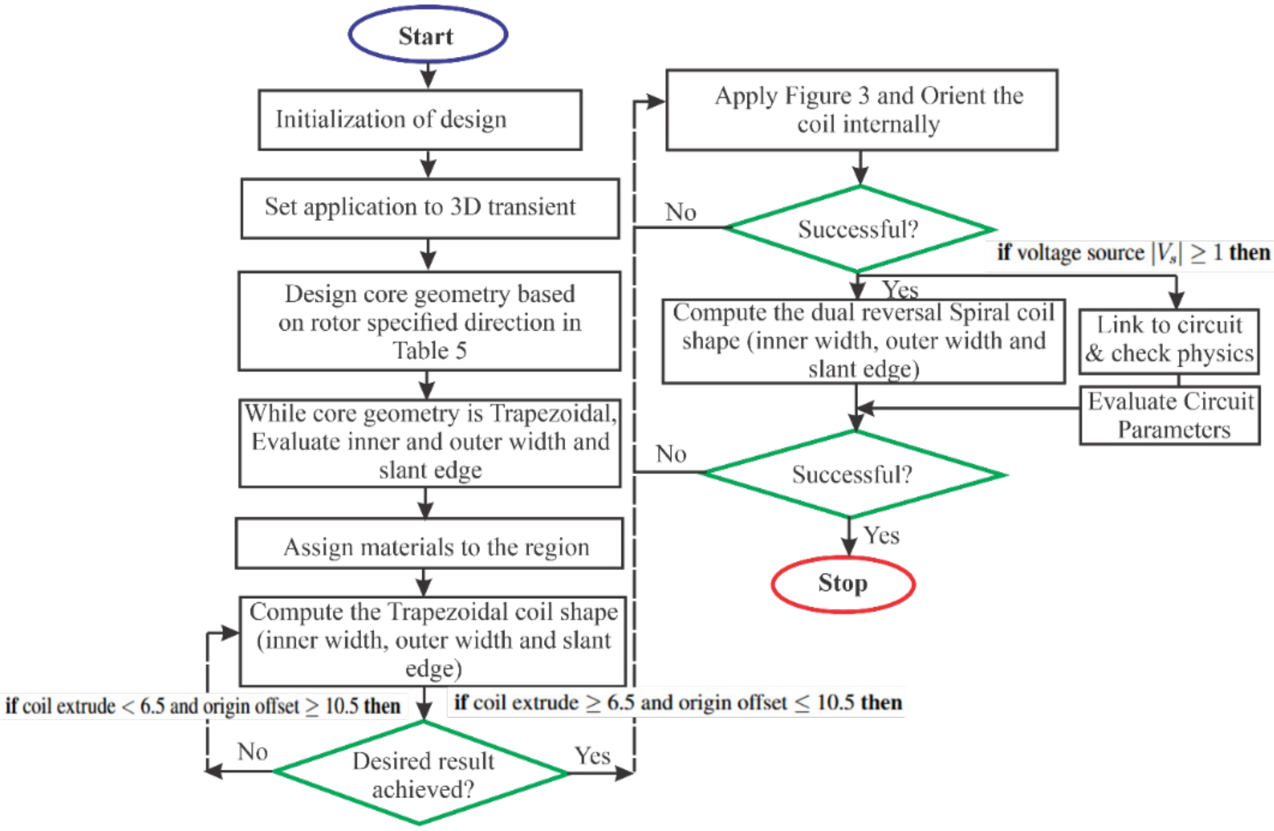

FIGURE 8. Electromagnet design Flowchart for TR-ELMAG and DR-ELMAG.

MATERIALS COMPOSITION FOR CAFEMG DESIGN

Material selection for the rotor, stator, coil encapsulation, and electromagnet core is based on thermal, mechanical, and electromagnetic requirements, as summarized in Table 6 (Reyes et al. 2023; Escobar et al. 2023; Liu et al. 2013). Bakelite and polyamide are selected for the rotor and stator support structures due to their low density (1,200–1,400 kg/m³), adequate tensile strength (100–120 N/mm²), and low thermal conductivity, which reduces parasitic heat transfer while maintaining mechanical stability. Epoxy resin is used for coil encapsulation owing to its high chemical resistance, comparable tensile strength, and sufficient heat deflection temperature (200 °C), ensuring structural integrity and electrical insulation under operating conditions.

For magnetic components, FLU-Copper is employed where controlled magnetic permeability and reduced mass are required. Its moderate density (5,200 kg/m³), heat deflection temperature (220 °C), and lower thermal conductivity compared to iron help limit eddy-current losses while maintaining acceptable mechanical strength. Iron is reserved for regions requiring high magnetic permeability and mechanical robustness, such as flux return paths, due to its superior tensile strength (350 N/mm²) and high thermal tolerance (500 °C), despite its higher density (7,800 kg/m³). This material combination balances electromagnetic performance, thermal stability, and structural integrity in the SSDR stator CAFEMG model.

TABLE 6. Material Properties Comparison

Properties	Rotor	Stator		Coil	Electromagnet Core
	Bakelite	Polyamide	Epoxy Resin	FLU-Copper	Iron (FLU_ M400_50A)
Overall Chemical Resistance	Excellent	Moderate	Excellent	High	Moderate
Specific Weight [kg/dm^3]	1.4	1.2	1.3	5.2	7.9
Heat Deflection Temperature under Load [°C]	200	150	200	220	500
Thermal Conductivity (W/mk)	0.5	0.3	0.5	15	80
Tensile Strength(N/mm^2)	120	100	120	80	350
Density (kg/m^3)	1400	1200	1300	5200	7800

RESULTS AND DISCUSSIONS

A comparative analysis of two electromagnet generator designs examines the electromagnetic performance influence at no load conditions within a rated speed of 500rpm at 50Hz . It assesses how each design handles flux uniformity, energy conversion efficiency, and torque characteristics, ultimately comparing power output to determine the better design for specific applications.

This section analyzes the simulation results of the mono-layer TR-SPC configuration paired with two electromagnet array variants, focusing on the impact of winding–core interactions on electromagnetic behavior and overall system performance are presented as follows.

AIRGAP MAGNETIC FLUX DENSITY

The 3D surface plots in Figure 9 depict the magnetic flux density distribution in the air gap of the rotating SSDR-CAFEMG along the radial and axial directions. For the TR-ELMAG configuration in Figure 9(a), the flux density ranges from 16.96 mT to 194.42 mT, peaking near a radial position of 1.745 mm at the axial center, with an average axial gradient of 3.55mT/mm and minimal radial variation. In contrast, the DR-ELMAG configuration in Figure 9(b) exhibits a higher peak flux density of 495.25 mT near the axial center at a radial position of 5 mm, with an axial gradient reaching 72 mT/mm. The flux density decreases by approximately 80% toward the axial extremes, while moderate radial variation indicates dominant sensitivity to axial displacement.

Notably, these results demonstrate that electromagnet design plays a critical role in shaping air-gap flux distribution and electromagnetic interaction, with the DR-ELMAG configuration yielding the most optimal distribution.

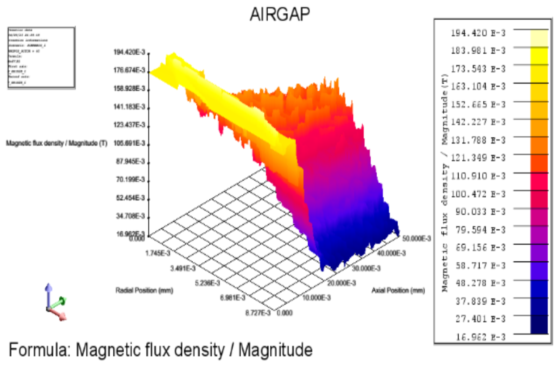

(a)

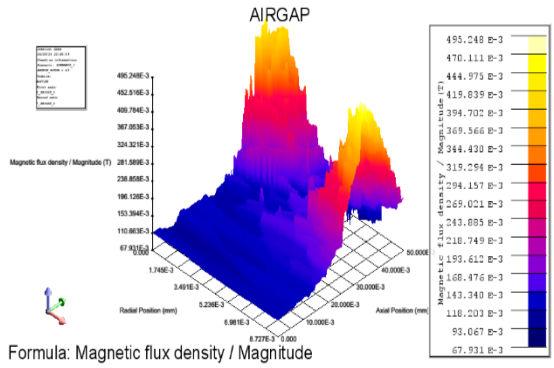

(b)

FIGURE 9. (a) Airgap flux density for TR-ELMAG Configuration. (b) Airgap flux density for DR-ELMAG Configuration

MAGNETIC FLUX AND MAGNETIC FILED DISTRIBUTION ON ELECTROMAGNETS

The electromagnetic performance of the SSDR CAFEMG is evaluated by examining the magnetic flux distribution of the TR-ELMAG. and DR-ELMAG electromagnets. As shown in Figure 10(a), TR-ELMAG exhibits flux density variations between 0.6 and 1.2T, corresponding to rotor pole interactions that contribute to torque ripple. Figure 10(b) shows that DR-ELMAG produces flux densities ranging from 0.6 to 1.8T, with peak values concentrated near the coil windings and rotor cores. These results provide insight into air-gap flux uniformity and core saturation indicating potential improvements.

Figures 10(c) and (d) display the distributions of flux density and corresponding magnetic field strength for the two setups of electromagnets. In Figure (c), the maximum magnetic field intensity approaches about 578.14 kA/m, with heightened field areas concentrated at the edges of the electromagnet core and winding connections, suggesting greater localized flux accumulation. In comparison, Figure 10(d) shows a significantly greater peak field intensity of around 990.19 kA/m, in contrast to Figure 10(c). Although the intensity has increased, the field distribution illustrated in Figure (d) shows a more consistent spatial uniformity in the circumferential direction, with less pronounced sharp gradients at the edges. This numerical distinction emphasizes that the second setup not only increases magnetic field strength but also enhances the consistency of flux distribution, helping to reduce local saturation and improve overall electromagnetic efficiency.

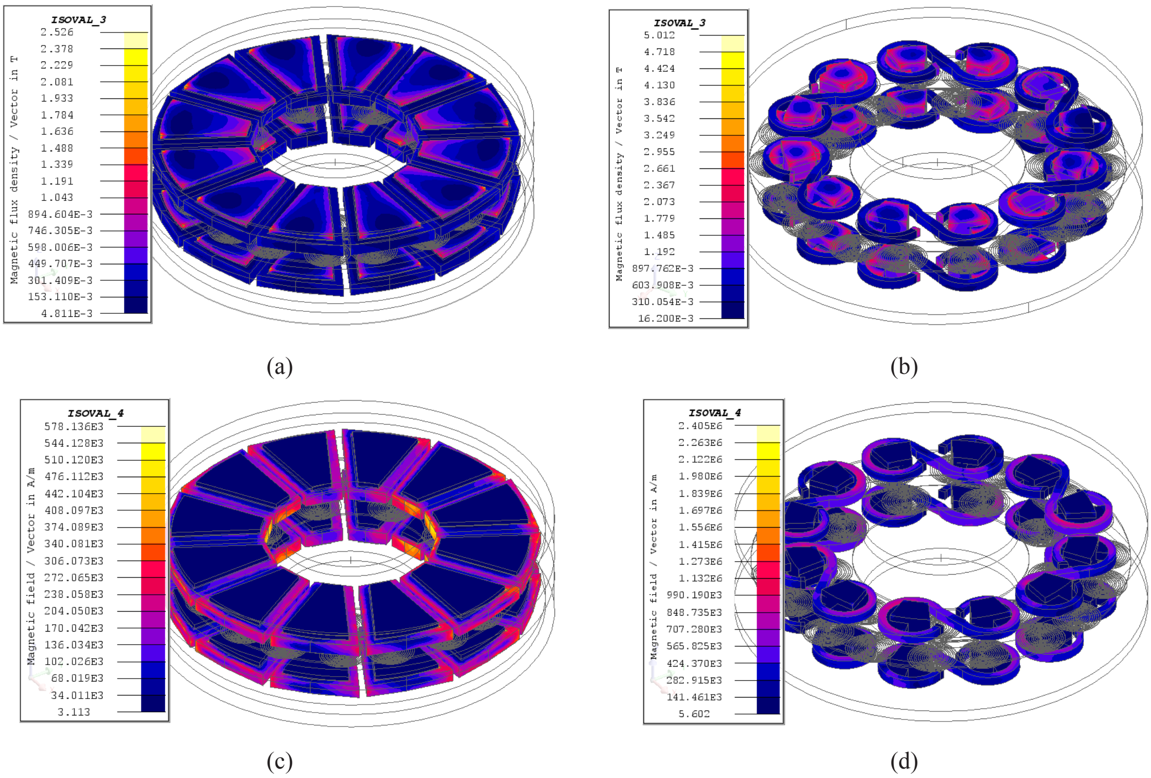

FIGURE 10. (a) Magnetic flux density distribution of Trapezoidal Electromagnet (TR-ELMAG) (b) Magnetic flux density distribution of Dual Reversal Spiral Electromagnet (DR-ELMAG). (c) Magnetic field distribution of Trapezoidal Electromagnet (TR-ELMAG) (d) Magnetic field distribution of Dual Reversal Spiral Electromagnet (DR-ELMAG).

TR-SPC COIL FLUX DENSITY AND MAGNETIC FIELD DISTRIBUTION

The coil flux density distribution for TR-ELMAG ranges from 0.821mT to 224.72mT, while DR-ELMAG ranges from 0.816mT to 478.65mT, with peak flux concentration near the stator windings and tri-arm junctions, as in Figures 11(a) and 11(b). In summary, these findings verify that the DR-ELMAG configuration produces more powerful and focused magnetic fields, resulting in better flux distribution and heightened electromagnetic interactions compared to the TR-ELMAG.

The magnetic field strengths shown in Figures 11(c) and 11(d) achieve maximum values of 178.87 kA/m for the TR-ELMAG and 380.90 kA/m for the DR-ELMAG, highlighting a significantly greater field strength in the DR-ELMAG setup and emphasizing the impact of electromagnet configuration.

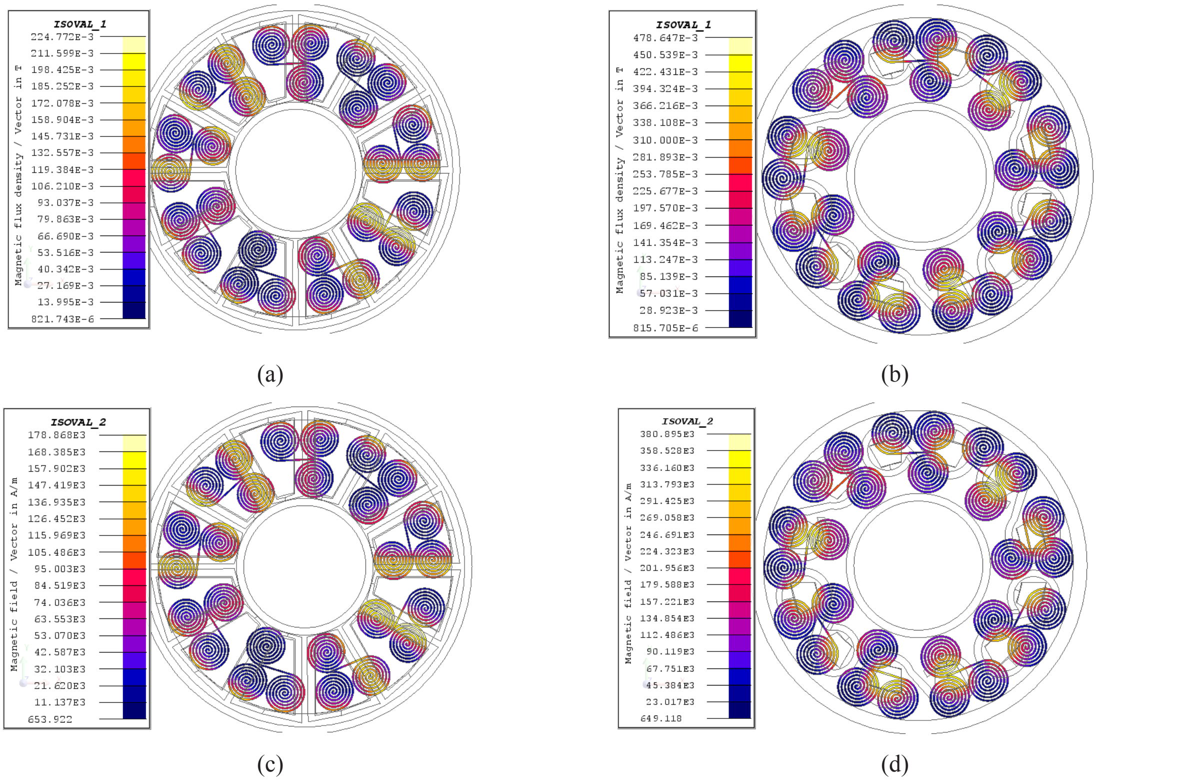

FIGURE 11: (a) TR-SPC Coil Magnetic flux density based on TR-ELMAG. (b) TR-SPC Coil Magnetic flux density based on DR-ELMAG. (c) TR-SPC Magnetic field distribution based on TR-ELMAG. (d) TR-SPC Coil Magnetic field distribution based on DR-ELMAG.

BEMF AND INDUCED CURRENT GENERATED FOR CAFEMG

Both models produce balanced three-phase sinusoidal back-EMF and induced current waveforms, although they do not perfectly overlap. The TR-ELMAG generates a peak back-EMF of approximately 35 V, whereas the DR-ELMAG achieves about 38 V, representing a 7.9% increase as depicted in Figure 12(a). However, phase 1 of the DR-ELMAG showed a noticeable transient distortion before stability was attained.

Correspondingly, the maximum current achieved is 3.1 A for TR-ELMAG and 3.2 A for DR-ELMAG, as clearly depicted in Figure 12(b), with both showing ideal sinusoidal shapes without any distortion. These results showed that the DR-ELMAG configuration outperforms the TR-ELMAG in terms of voltage and current generation, emphasizing the advantages of its electromagnet design.

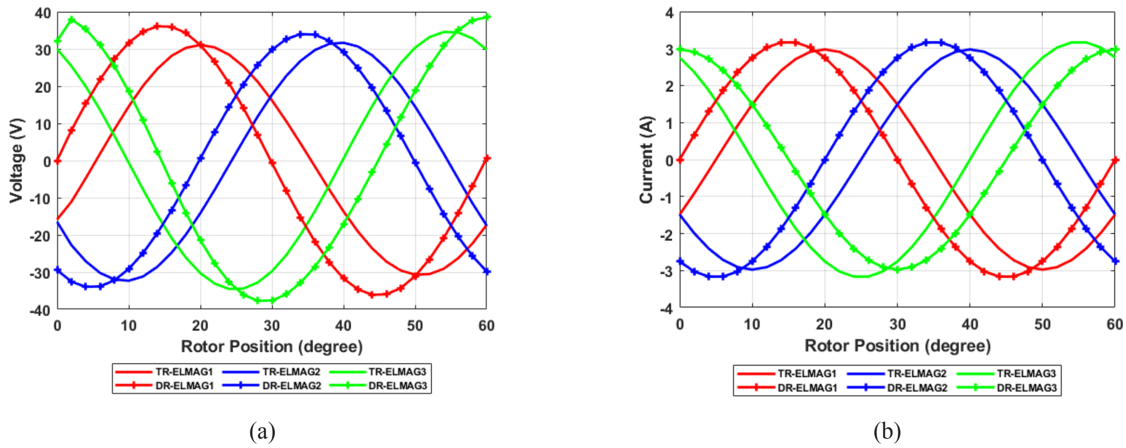

FIGURE 12: (a) BEMF for CAFEMG employing TR-ELMAG and DR-ELMAG (b) Induced Current for CAFEMG employing TR-ELMAG and DR-ELMAG

BEMF HARMONIC SPECTRUM

Figure 13(a) and (b) compare the voltage harmonic spectra of the CAFEMG-based TR-ELMAG and DR-ELMAG configurations. The TR-ELMAG exhibits higher magnitudes of the 5th and 7th harmonics, reaching approximately 0.30 V, indicating increased harmonic distortion. In contrast, the DR-ELMAG shows significantly reduced higher-order harmonic content, with harmonic magnitudes below 0.06 V, corresponding to a reduction of over 80% compared to the TR-ELMAG. This quantitative reduction in higher-order harmonics demonstrates the superior waveform quality and lower distortion achieved by the DR-ELMAG configuration.

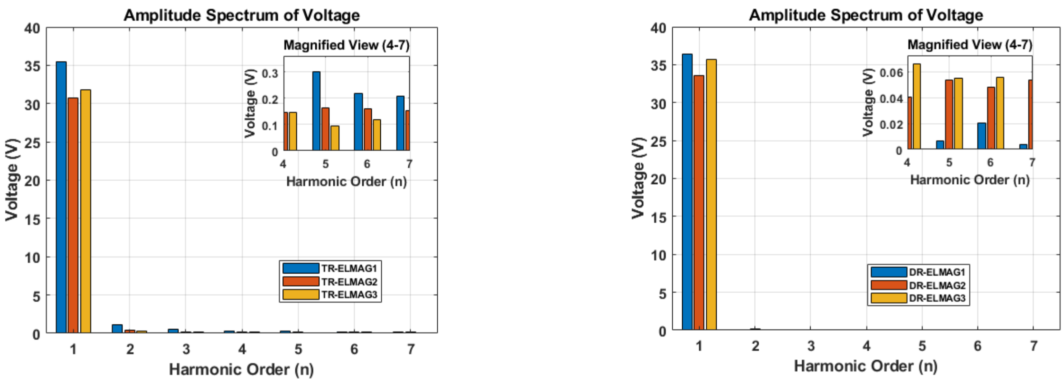

(a) (b)

FIGURE 13. (a) Harmonic spectrum for CAFEMG-based TR-ELMAG (b) Harmonic spectrum for CAFEMG-based DR-ELMAG

COIL FLUX LINKAGE DISTRIBUTION

Figure 14 depicts the coil flux linkage characteristics and respective harmonic distortion of the SSDR-CAFEMG for the TR-ELMAG and DR-ELMAG configurations. As shown in Figure 14(a), both models exhibit nearly sinusoidal flux linkage waveforms with good phase alignment; however, the DR-ELMAG achieves a slightly higher peak flux linkage of approximately 2.0 mWb, compared to about 1.8 mWb for the TR-ELMAG, indicating enhanced magnetic coupling. Notably, the obtained results are comparable to those reported for existing planar coil configurations; however, further improvements are expected through the optimization of key geometric parameters, particularly the inner-to-outer diameter ratio.

For the TR-ELMAG, the resulting estimated flux linkage total harmonic distortion (THD) is approximately 1.1% with lower fundamental harmonic. In contrast, the DR-ELMAG exhibits significantly lower higher-order harmonic content, corresponding to a reduced THD of about 0.5%. This represents a reduction of more than 50% in flux linkage distortion, confirming that the DR-ELMAG configuration achieves improved magnetic coupling.

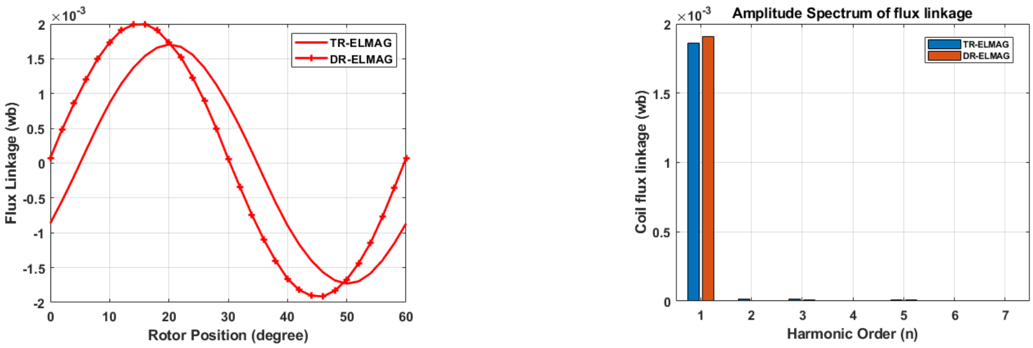

(a) (b)

FIGURE 14. (a)2D plot for a coil flux linkage based on SSDR CAFEMG. (b) Coil flux linkage harmonic distortions on SSDR CAFEMG-based TR-ELMAG and DR-ELMAG

TORQUE AND COGGING TORQUE

The output torque in Figure 15(a) for the Proposed TR-ELMAG exhibits a smoother torque profile ranging from 0.25 Nm to -0.55 Nm with minor fluctuations generated averaged torque of 0.18Nm, while Proposed DR-ELMAG experiences significant variations between 0.45 Nm and -2.75 Nm, indicating higher averaged torque of 1.15Nm, resulting in a lower torque ripple of 2.8% in contrast to the 5.8% produced by the former with the potential mechanical stress.

Cogging torque in electromagnet-based generator can arise from periodic air-gap reluctance variations caused by iron core geometry rather than from permanent magnets alone. As shown in Figure 15(b), the TR-ELMAG configuration exhibits cogging torque fluctuations ranging from approximately 1.4 to −2.0 mNm, resulting in a peak-to-peak value of about 3.4 mNm. This behavior is attributed to the geometrical dimension of discrete electromagnet iron cores, which generate non-uniform magnetic attraction forces as the rotor moves, leading to measurable cogging torque.

In contrast, DR-ELMAG exhibits an approximately 0 Nm cogging torque due to its symmetrically distributed dual iron core arrangement accompanied by reduced geometrical dimension, which effectively balances magnetic forces throughout rotation. This near-zero cogging torque contributes to improved efficiency, reduced vibration, and enhanced operational stability, making the DR-ELMAG a preferable design for smoother and more reliable generator performance.

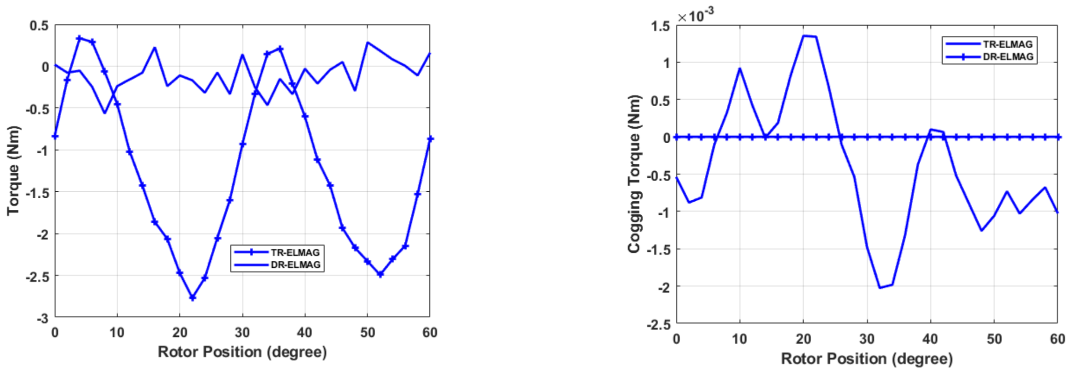

(a) (b)

FIGURE 15. (a) Torque of TR-ELMAG and DR-ELMAG. (b) Cogging torque of TR-ELMAG and DR-ELMAG

POWER GENERATED IN SSDR-CAFEMG

Figure 16 illustrates the power output of the two proposed models, TR-ELMAG and DR-ELMAG, over a rotor position range of 0-60°. The DR-ELMAG achieves an average power output of approximately 166 W, while the TR-ELMAG delivers about 164 W. This indicates that the DR-ELMAG produces a slightly higher average power output, corresponding to an improvement of approximately 1.2% compared to the TR-ELMAG.

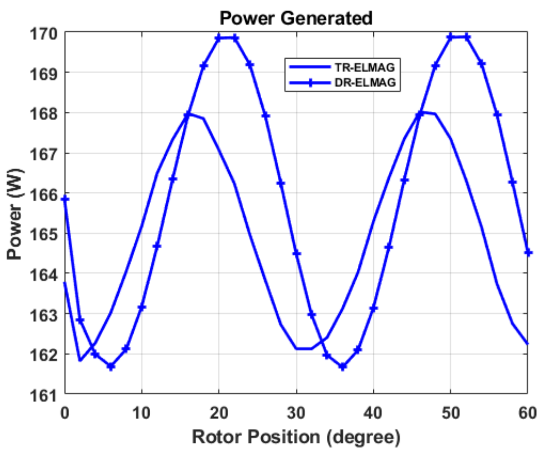

FIGURE 16. Power distribution across TR-ELMAG and DR-ELMAG, respectively

COMPARATIVE ANALYSIS

The comparative analysis is displayed in Table 7 for both models and other literature. It offers a captivating comparison of the SSDR-based magnet and electromagnet generators' design. The comparison between magnet-based and electromagnet-based configurations is based on key electromagnetic and performance parameters, including coil and excitation arrangement, air-gap and coil flux characteristics, flux linkage, back-EMF and its harmonic distortion, current, torque (average and cogging), output power, speed, and overall efficiency. The proposed design effectively addresses some key limitations identified in previous studies.

TABLE 7. Comparison of performance parameters between magnet-based and electromagnet-based generators.

Parameters	Units	Habib et al. (2020)	Frank and Laksar (2021)	Alsuwian et al. (2024)	Marcolini et al. (2023)	Pranjic and Virtic (2020)	Tsunata et al. (2022)	TR-ELMAG	DR-ELMAG
Number of coils	-	18	9	9	12	6	24	9	9
Coil turns	-	250	18	1050	64		46	18	18
Number of Magnets	-	60	24	60	20	20	10	-	-
Number of electromagnets	-	-	-	-	-	-	-	12	12
Airgap flux density	mT							194.42	495.25
Peak electromagnet flux density	T	-	-	-	-	-	-	1.2	1.8
Electromagnet field distribution	kA/m	-	-	-	-	-	-	578.14	990.19
TR-SPC coil flux density	mT	-	-	-	-	-	-	224.72	478.65
TR-SPC coil magnetic field distribution	kA/m	-	-	-	-	-	-	178.87	380.90
Flux linkage	mWb							1.8	2.0
Speed	rpm	500	500	500	15000	600	6000	500	500
BEMF	V	208		230	13.5	33.97	230	35	39
BEMF THD								1.2	0.6
Current	A	5.6		2.5	25	20.19	-	3.1	3.2
Average torque	Nm	28.85	-	29.2	30m	30.97	0.8	0.18	1.15
Cogging torque (Tpk2pk)	mNm	-	-	-	-	-	-	3.40	0.00
Output power	W	1510	200	1410	1000	-	-	164	166
Losses	W							16	14
Efficiency	%	-	-	92.2	>87	-	96	91.1	92.2

Similarly, Figure 17 shows the performance evaluation parameters of the CEFEMG-based DR-ELMAG and TR-ELMAG configurations in terms of output power, efficiency, and losses as presented in equations (17) - (20). However, the DR-ELMAG demonstrated improved efficiency over TR-ELMAG with 92.20 against 91.1%. Correspondingly, the DR-ELMAG exhibits losses of 7.8%, in contrast to 8.9% for TR-ELMAG, which is primarily contributed by copper loss, bearing loss, eddy current loss, and core loss. These results indicate a marginal increase in output power, resulting in superior energy utilization and reduced loss characteristics for the DR-ELMAG configuration.

$$\eta = \frac{P_o}{P_o + (L_{osses})} \times 100 \tag{17}$$

$$L_{osses} = \frac{P_g - P_o}{P_g} \times 100 \quad (18)$$

$$L_{osses} = P_{cu} + P_{be} + P_{hy} + P_{ed} \quad (19)$$

$$L_{osses} = 3I^2R + C_f\omega_m^3 + (K_h f B_p^{1.6} + K_e f^2 B_p^2) \quad (20)$$

Where; P_o is the generator output power, P_{cu} gives the copper loss, P_{be} is defined as the mechanical bearing loss. Losses due to the core are formulated as hysteresis and eddy current losses (P_{hy} and P_{ed}) respectively. Additionally, K_h, K_e are the hysteresis loss coefficient and the eddy current loss coefficient with a value of $20*10^{-4}$ and 10^{-4}. Notably, f is the frequency, and B_p is the TRS-PC peak flux density; the mechanical speed is given by ω_m and C_f is defined as 10^{-4} and 10^{-5} for the air friction of single-core and dual-core trapezoidal geometries, respectively.

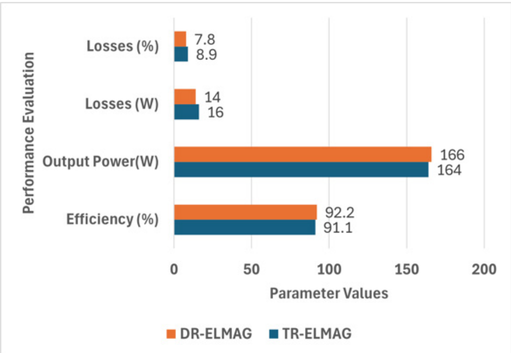

Figure 17. Performance comparison for the proposed SSDR CAFEMG

CONCLUSION

This study demonstrates a significant advancement in pico-scale generator technology through the optimization of a dual-rotor, stator-coreless axial flux electromagnet generator (CAFEMG) employing single-layer trapezoidal spiral planar coils (TR-SPC) with non-overlapping concentrated windings. The integration of electromagnet variants namely trapezoidal electromagnets (TR-ELMAG) and dual-reversal spiral electromagnets (DR-ELMAG) effectively reinforces the inherently non-ideal sinusoidal flux density distribution associated with planar winding structures. The electromagnetic enhancement is evidenced by the substantial increase in air-gap flux density from 194.42 mT in TR-ELMAG to 495.25 mT in DR-ELMAG, alongside higher peak electromagnet flux density (1.8 T versus 1.2 T), coil flux density (478.65 mT versus 224.72 mT), and electromagnet field distribution (990.19 kA/m versus 578.14 kA/m). These improvements directly contribute to enhanced voltage generation (39 V versus 35 V) and stable current output under comparable operating conditions of 500rpm at 50Hz.

Comparative performance evaluation confirms that the DR-ELMAG configuration consistently outperforms the TR-ELMAG across key electromagnetic and electromechanical metrics. Notably, DR-ELMAG delivers a significantly higher average torque of 1.15 Nm compared to 0.18 Nm, improved back-EMF magnitude, increased flux linkage (2.0 mWb versus 1.8 mWb), and superior efficiency of 92.2%, surpassing 91.1% obtained in TR-ELMAG, while eliminating cogging torque, in contrast to the 3.4 mNm observed in the TR-ELMAG configuration.

From an application standpoint, the enhanced airgap and coil magnetic field distributions, including the improved TR-SPC coil magnetic field strength of up to 380.90 kA/m, translate directly into higher power of 166W for DR-ELMAG with 14W of loss as against 164Wfor TR-ELMAG accompanied with 16W resulting in an improved energy conversion efficiency. These characteristics make the DR-ELMAG-based CAFEMG especially suitable for decentralized renewable energy systems, particularly rural and off-grid pico-hydro installations where compactness, reliability, and low maintenance requirements are critical.

Nevertheless, this study does not consider thermal behavior, effects of current density, detailed mechanical losses, or the long-term reliability of insulation in multilayer electromagnet windings. Subsequent efforts will concentrate on manufacturing prototypes, validating them through load-based experiments, optimizing multi-disk and multi-layer windings, and developing detailed thermal models along with suitable cooling methods to improve the performance, longevity, and practical usability of the suggested generator design.

ACKNOWLEDGEMENT

The authors acknowledge Centre for Post Graduate Studies and Universiti Teknologi PETRONAS for providing a registered AlTAIR flux software. Author Isiaka, is grateful to Petroleum Technology Development Fund (PTDF), Nigeria for his PhD research sponsorship under the grant PTDF/ED/OSS/PHD/IS/1694/20.

DECLARATION OF COMPETING INTEREST

None.

REFERENCES

Aghapour, O., Azari, M. N. & Mirimani, S. M. 2023. Influence of different rotor positions on the performance of a coreless axial-flux generator. In *2023 14th Power Electronics, Drive Systems, and Technologies Conference (PEDSTC 2023)*, pp. 1-5. https://doi.org/10.1109/PEDSTC57673.2023.10087130

Alsuwian, T. et al. 2024. Prototype development of a fully coreless multi-stage axial-flux permanent-magnet machine (AFPM) through the performance comparison between single-stator double-rotor (SSDR) and double-stator single-rotor (DSSR) configurations. *Alexandria Engineering Journal* 92: 283-293. https://doi.org/10.1016/j.aej.2024.02.023

Alsuwian, T. M. et al. 2025. Six-phase fully coreless axial-flux permanent-magnet generator: Design, fabrication, and performance analysis. *IEEE Access* 13: 22647-22655. https://doi.org/10.1109/ACCESS.2025.3526165

Chulaee, Y. & Ionel, D. M. 2024. Ultra-fast finite element analysis of coreless axial flux permanent magnet synchronous machines. *IET Electric Power Applications*: 1-14. https://doi.org/10.1049/elp2.12439

Chulaee, Y., Mohammadi, A., Cramer, A. M. & Ionel, D. M. 2024. Sensorless control of low inductance coreless AFPM machines for fault-tolerant operation of propulsion systems. In *2024 IEEE Transportation Electrification Conference and Expo (ITEC)*, pp. 1-5. IEEE. https://doi.org/10.1109/ITEC60657.2024.10598978

Devred, A., Ballarino, A., Bourcey, N., Mangiarotti, F., Milanese, A. & Petrone, C. 2024. Proof-of-principle of an energy-efficient, iron-dominated electromagnet for physics experiments. *IEEE Transactions on Applied Superconductivity* 34(5). https://doi.org/10.1109/TASC.2024.3355872

El-Hasan, T. S. 2023. Air-cored axial flux permanent magnet generator for direct driven micro wind turbines. *IET Renewable Power Generation* 17: 3687-3700. https://doi.org/10.1049/rpg2.12880

Escobar, A., Sánchez, G., Jara, W., Madariaga, C., Tapia, J. A., Riedemann, J. & Reyes, E. 2023. Impact of manufacturing tolerances on axial flux permanent magnet machines with ironless rotor core: A statistical approach. *Machines* 11: 535. https://doi.org/10.3390/machines11050535

Frank, Z. & Laksar, J. 2021. Analytical design of coreless axial-flux permanent magnet machine with planar coils. *IEEE Transactions on Energy Conversion* 36: 2348-2357. https://doi.org/10.1109/TEC.2021.3050502

Gao, B. et al. 2024a. Optimal design of PCB coreless axial flux permanent magnet synchronous motor with arc windings. *IEEE Transactions on Energy Conversion* 39: 567-577. doi: 10.1109/TEC.2023.3315413.

Gao, H., Huang, W., Zhang, Z. & Wang, C. 2024b. Torque improvement of dual-rotor coreless stator AFPM machine with non-overlapping concentrated winding for counter-rotating ducted fan application. *IEEE Transactions on Transportation Electrification* 10: 9501-9512. doi: 10.1109/TTE.2024.3351853.

Habib, A., Che, H. S., Abd Rahim, N., Tousizadeh, M. & Sulaiman, E. 2020. A fully coreless multi-stator multi-rotor (MSMR) AFPM generator with combination of conventional and Halbach magnet arrays. *Alexandria Engineering Journal* 59: 589-600. doi: 10.1016/j.aej.2020.01.039.

Huang, R., Dong, Z., Liu, Y., Liu, S. & Liu, C. 2023. A novel concentric winding axial-flux permanent magnet machine with high winding factor. In IECON Proceedings (Industrial Electronics Conference), pp. 1-6. IEEE. https://doi.org/10.1109/IECON51785.2023.10312466

Khan, S., Bukhari, S. S. H. & Ro, J.-S. 2019. Design and analysis of a 4-kW two-stack coreless axial flux permanent magnet synchronous machine for low-speed applications. *IEEE Access* 7: 173848-173854. doi: 10.1109/ACCESS.2019.2957046.

Lijesh, K. P. & Hirani, H. 2015. Design and development of Halbach electromagnet for active magnetic bearing. *Progress in Electromagnetics Research C* 56.

Liu, J. Z., Wang, Y. J., Chen, T., Pan, M. Q., Chen, L. G. & Sun, L. N. 2013. On study of high speed permanent magnet synchronous motor without iron core. *Advanced Materials Research* 706-708: 882-887. doi: 10.4028/www.scientific.net/AMR.706-708.882.

Marcolini, F., De Donato, G., Giulii Capponi, F., Incurvati, M. & Caricchi, F. 2023. Novel multiphysics design methodology for coreless axial flux permanent magnet machines. *IEEE Transactions on Industry Applications* 59: 3220-3231. doi: 10.1109/TIA.2023.3241891.

Minaz, M. R. & Çelebi, M. 2017. Design and analysis of a new axial flux coreless PMSG with three rotors and double stators. *Results in Physics* 7: 183-188. doi: 10.1016/j.rinp.2016.10.026.

Mohd Nasir, N. N., Mohamed Haris, S. & Mat Tahir, M. F. 2025. Simulation of pole slip control in an axial flux magnetic gear with changeable transmission ratios using Stateflow and Simulink. *Jurnal Kejuruteraan* 37(4): 2015-2024. https://doi.org/10.17576/jkukm-2025-37(4)-38

Ouldhamrane, H., Charpentier, J.-F. F., Khoucha, F., Zaoui, A., Achour, Y. & Benbouzid, M. 2022. Development and experimental validation of a fast and accurate field calculation tool for axial flux permanent magnet machines. *Journal of Magnetism and Magnetic Materials* 552: 169105. doi: 10.1016/j.jmmm.2022.169105.

Pranjic, F. & Virtic, P. 2020. Designing rotor disks of a coreless axial flux permanent magnet machines by using simplified FEM and an approximation method. *IEEE Transactions on Energy Conversion* 35: 1505-1512. doi: 10.1109/TEC.2020.2977965.

Reyes, N. et al. 2023. Structural feasibility and electromagnetic analysis of an ironless rotor axial flux permanent magnet synchronous machine. In *2023 IEEE Energy Conversion Congress and Exposition (ECCE 2023)*, pp. 4297-4301. doi: 10.1109/ECCE53617.2023.10362936.

Shang, J., Zhang, H., Yao, T., Zhao, M. & Cheng, D. 2024. A novel stator coreless disk motor with skewed wave winding for shaftless rim thruster. *IEEE Transactions on Applied Superconductivity*: 1-5. doi: 10.1109/TASC.2024.3468189.

Shuaibu, I. et al. 2024a. State-of-art review of renewable energy-based systems for electrical machine applications: Prospects and challenges. In *IOP Conference Series: Earth and Environmental Science* 1365: 012005. https://doi.org/10.1088/1755-1315/1365/1/012005

Shuaibu, I., Ho, E. H. T. W., Kannan, R. & Samaila, Y. A. 2024b. Advancements in axial flux permanent magnet machines utilizing coreless technology: A systematic review. *Ain Shams Engineering Journal* 15: 103091. doi: 10.1016/j.asej.2024.103091.

Shuaibu, I., Ho, E. H. T. W., Kannan, R. & Samaila, Y. A. 2025. The utilization of printed circuit boards (PCBs) in axial flux machines: A systematic review. In *ASEC 2024* 13. Basel: MDPI. https://doi.org/10.3390/engproc2025087013

Shuaibu, I. & Ho, E. T. W. 2023. Investigation of a spiral planar coil on coreless axial flux PM generator for pico-hydro applications. In *2023 IEEE Conference on Energy Conversion (CENCON)*, pp. 58-63. IEEE. https://doi.org/10.1109/CENCON58932.2023.10369297

Szelag, W., Jedryczka, C., Baranski, M. & Kurzawa, M. 2024. Design, analysis and experimental verification of a coreless permanent magnet synchronous motor. *Energies* 17. doi: 10.3390/en17071664.

Tsunata, R., Takemoto, M., Ogasawara, S., Saito, T. & Ueno, T. 2022. SMC development guidelines for axial flux PM machines employing coreless rotor structure for enhancing efficiency based on experimental results. *IEEE Transactions on Industry Applications* 58: 3470-3485. doi: 10.1109/TIA.2022.3154336.

Wang, X., Li, T., Cui, X. & Zhao, X. 2022. Design and analysis of coreless axial flux permanent magnet machine with novel composite structure coils. *Energies* 15: 5162. doi: 10.3390/en15145162.

Yao, K., Ye, C. C., Wan, S., Liu, K., Ye, C. C. & Zhu, D. 2023. Research on new coreless axial flux high speed permanent magnet synchronous motor for flywheel energy storage. In *2023 26th International Conference on Electrical Machines and Systems (ICEMS 2023)*, pp. 1143-1148. doi: 10.1109/ICEMS59686.2023.10344482.

Zaihidee, F. M., Mubin, M., Che, H. S. & Rui, T. J. 2022. Development of closed-loop permanent magnet synchronous motor drive system prototype. *Jurnal Kejuruteraan* 5(2 Special Issue): 79-90. https://doi.org/10.17576/jkukm-2022-si5(2)-09

Zhang, W., Lin, F., Chen, H., Wang, Y. & Liu, C. 2023. Electromagnetic design and performance analysis of coreless superconducting machine. *Energy Reports* 9: 1000-1010. doi: 10.1016/j.egyr.2023.04.167.

Zhu, R., Tong, X., Han, Q., He, K., Wang, X. & Wang, X. 2023. Calculation and analysis of unbalanced magnetic pull of rotor under motor air gap eccentricity fault. *Sustainability* 15: 8537. doi: 10.3390/su15118537